Fusion and elastic scattering for the $^{12}C+^{144}Sm$ system at energies near to the Coulomb barrier

D. Abriola, A. A. Sonzogni, M. di Tada, A. Etchegoyen, M. C. Etchegoyen, J. O. Fernández Niello, S. Gil, A. O. Macchiavelli, A. J. Pacheco, R. Piegaia,* and J. E. Testoni
TANDAR, Departamento de Física, Comisión Nacional de Energía Atómica, Avenida del Libertador 8250, 1429 Buenos Aires, Argentina
(Received 30 January 1992)

Fusion cross sections have been measured for $^{12}C+^{144}Sm$ at bombarding energies in the range $46.5 \leq E_{lab} \leq 75$ MeV by off-line observations of x rays and gamma rays emitted in the decay of the evaporation residues and their daughters. Elastic scattering angular distributions for the same system have also been measured in the range $49 \leq E_{lab} \leq 63$ MeV. These data were used to obtain the parameters of an optical-model potential. It was found that a simultaneous description of both elastic scattering and fusion leads to an energy-dependent potential, with its real and imaginary parts connected by a dispersion relation.

PACS number(s): 25.70.Jj, 25.70.Bc

I. INTRODUCTION

Elastic scattering and total reaction cross sections are usually interpreted in terms of the optical model, where a complex potential is used to take into account absorptive processes. The imaginary component of this potential is often considered as the sum of two separate contributions: a surface term, to describe peripheral reactions (inelastic and transfer channels), and a volume term, which describes deeper reactions (fusion). Since in general the optical-model parameters might vary with energy, their complete determination requires the measurement of the cross sections for fusion and angular distributions for elastic, inelastic, and transfer reactions at different energies. In addition, such determination would be a test of reliability for the optical model.

Near-barrier measurements are particularly interesting because fusion, inelastic, and transfer cross sections decrease rapidly for energies below the barrier, therefore the surface imaginary part of the potential must also decrease. In a study of the $^{16}O+^{144}Sm$ system, it has been reported [1] that such variations of the imaginary component induce changes in the real part of the potential which are governed by dispersion relations. In this work, the $^{12}C+^{144}Sm$ system has been selected to continue those studies. Relative yields for evaporation-residue production for this system have been measured at energies above the barrier [2]. In the present work absolute evaporation-residue cross sections are measured, as well as elastic scattering angular distributions at energies above and below the barrier.

II. EXPERIMENTAL METHOD

Two different experiments were carried out to measure the evaporation-residue cross sections and the elastic scattering angular distributions, both of them at energies around the Coulomb barrier ($V_C = 50$ MeV in the laboratory frame). The experimental techniques are similar to those described in Refs. [1,3,4]. Beams of ^{12}C were provided by the 20 UV tandem accelerator at the TANDAR Laboratory in Buenos Aires, with energies in the range 46.5 to 75 MeV for fusion and 49 to 63 MeV for elastic scattering measurements. These beams were used to bombard an isotopically enriched (99%) target of ^{144}Sm with thickness of 90 $\mu g/cm^2$, evaporated onto a thin carbon backing of 30 $\mu g/cm^2$. The target was mounted in a scattering chamber, where two silicon surface-barrier detectors were placed at $\pm 30°$ with respect to the beam direction for normalization purposes. The beam was collected in a Faraday cup and its intensity during the bombardments, typically 10–15 particles nA, was recorded by multiscaling the integrated current in 1-min intervals.

A. Fusion

Thin aluminium catcher foils were placed behind the target. These catchers had the appropriate thickness (≈ 1.6 mg/cm^2) to stop the evaporation residues produced in the fusion of ^{12}C with ^{144}Sm, but not the products of the other reactions induced by the projectile on the carbon and the aluminium foil itself.

For each energy, after an irradiation of about two hours, the catcher was removed from the scattering chamber and placed in front of a 5 cm^3 high-purity Ge detector (with an energy resolution of 500 eV at 50 keV). This operation took about 5 min. Then, eight spectra of 5 min time interval and eight of 10 min were automatically recorded. An energy spectrum taken after a bombardment at $E_{lab} = 68$ MeV is shown in Fig. 1. In order to verify that no residual nuclei of interest could escape from the catcher, a second catcher, placed behind the first one during the irradiation at the highest bombarding energies, was measured under similar conditions. The areas of the $K\alpha_1$ and $K\alpha_2$ peaks in the energy spectra were obtained with the computer code GASPAN [5] and then corrected by the detector efficiency and electronic dead time. The absolute efficiency of the Ge detector was

*Departamento de Física, FCEyN, Universidad de Buenos Aires, Ciudad Universitaria, 1429 Buenos Aires, Argentina.

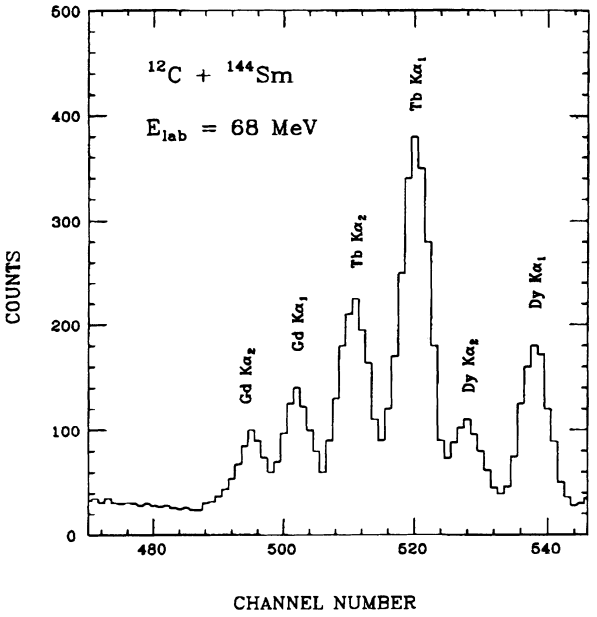

FIG. 1. X-ray and gamma-ray spectrum from the radioactive decay of evaporation residues after 120 min bombardment with ^{12}C at $E_{lab}=68$ MeV.

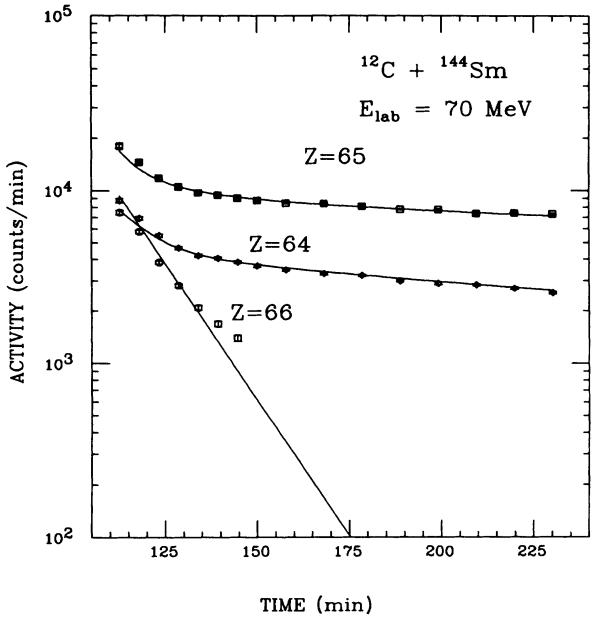

FIG. 3. The $K\alpha$ x-ray count rates from Dy, Tb, and Gd as a function of the time at $E_{lab}=70$ MeV. The curves are simultaneous fits of the data as described in the text.

determined by using a set of calibrated radioactive sources, which were mounted in the same geometry as the catcher. Corrections for electronic dead time were determined by using a pulse generator. The error in the areas was estimated to be about 4–6%. Figures 2 and 3 show $K\alpha$ x-ray activities of Dy, Tb, and Gd as a function of the time for $E_{lab}=52$ and 70 MeV, respectively.

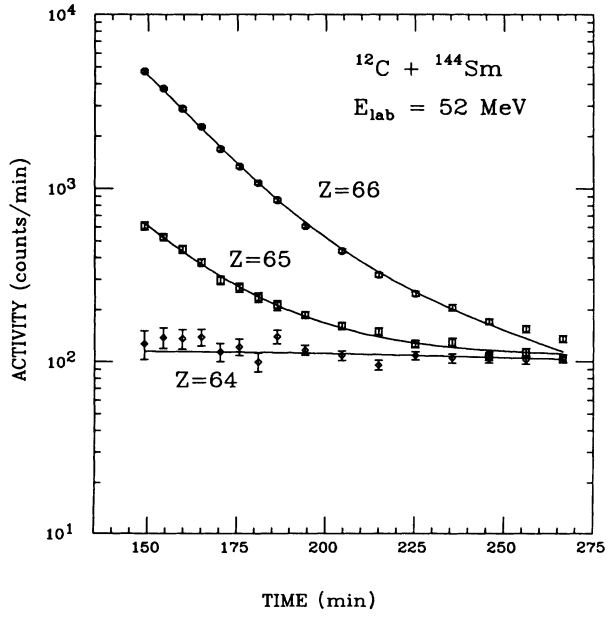

FIG. 2. The $K\alpha$ x-ray count rates from Dy, Tb, and Gd as a function of the time at $E_{lab}=52$ MeV. The curves are simultaneous fits of the data as described in the text.

Calling σ_A the cross section of each exit channel and taking into account the contribution from different decay chains, the counting rate of the $K\alpha$ x-rays in the interval defined by T_i and T_f can be calculated as follows:

$$A_Z(T_i,T_f)=\sum_A \sigma_A W_{Z,A} F_{Z,A}(T_{1/2},T_i,T_f) . \quad (1)$$

The function $F_{Z,A}(T_{1/2},T_i,T_f)$ is proportional to the integral between T_i and T_f of the activity for the decay of the nucleus (Z,A), $T_{1/2}$ are known half-lives (from Ref. [6]), and $W_{Z,A}$ are the number of $K\alpha$ x rays produced per decay of each isotope in each mass chain (from Ref. [7]). In comparing the experimental data with the calculated intensities, the σ_A values were taken as adjustable parameters in a least-squares procedure. These calculations were performed using the code XRAY [8]. The values of σ_A thus obtained were used to determine the fusion cross section σ as follows:

$$\sigma=\sum_A \sigma_A . \quad (2)$$

Identification of gamma transitions allows one to overcome some of the difficulties that arise in the determination of σ since some of the values of W are not always available. As an example, it was found in Ref. [7] that $W_{67,154}$ was 23, and the relative intensity of $K\alpha$ lines for the decay of ^{153}Ho was 470 (i.e, the absolute value of $W_{67,153}$ was unknown). An independent way to evaluate these W factors is to use the measured γ-ray activities to determine the cross sections for the $2n$ channel, and then adjust $W_{67,154}$ and $W_{67,153}$ to get a good agreement between the cross sections obtained from x rays and those from γ rays. The best adjusted values were $W_{67,154}=60\pm10$ and $W_{67,153}=35\pm5$.

The full curves in Figs. 2 and 3 are simultaneous fits to the activities for the second, third, and fourth generations of the decay chains (Dy, Tb, and Gd, respectively). Proton emission after compound-nucleus formation could not be distinguished from neutron evaporation due to the fact that the half-lives of the latter were short compared with the dead time between the end of the irradiation and the beginning of the measurement. Hence, only α-particle and neutron emission were considered in the calculation. The resulting fusion cross sections as a function of the bombarding energy are displayed in Fig. 4. It should be noticed that the present cross sections are about 30% higher than those reported in Ref. [2]. Perhaps this is due to the fact that the experimental method used in Ref. [2] does not allow an absolute normalization and the high energy data were scaled to a calculation. The present results also extend the lowest measured cross sections more than two orders of magnitude below previous measurements.

B. Elastic scattering

Elastically scattered ^{12}C particles from the ^{144}Sm target were detected by a set of four surface-barrier Si detectors. In order to optimize the energy resolution, the target angle was varied as a function of the detection angle. A typical energy spectrum at $E_{lab}=58$ MeV and $\theta_{lab}=140°$ is shown in Fig. 5. The elastic peak is well separated from the peaks of the reactions $^{144}Sm(^{12}C,^{12}C)^{144}Sm^*$, $^{144}Sm(^{12}C,^{12}C^*)^{144}Sm$, $^{144}Sm(^{12}C,^{11}C)^{145}Sm$. Angular distributions were taken at $E_{lab}=49$, 50, 51, 52, 53, 54, 58, and 63 MeV, some of which are shown in Figs. 6 and 7. The most important sources of errors arise from the uncertainties in the peak areas (essentially statistical) and in the position and solid angle of the detectors. All these contributions were estimated to be around 8%. The elastic scattering of $^{12}C+^{197}Au$ was measured at several energies to provide an independent check of the solid angles and angular positions of the detectors.

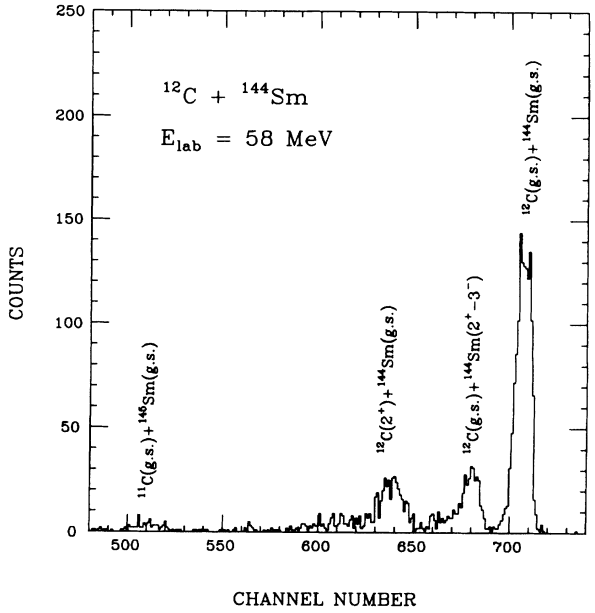

FIG. 5. Energy spectrum of the reaction products for $^{12}C+^{144}Sm$, measured at $E_{lab}=58$ MeV and $\theta_{lab}=140°$. Exit channels are indicated.

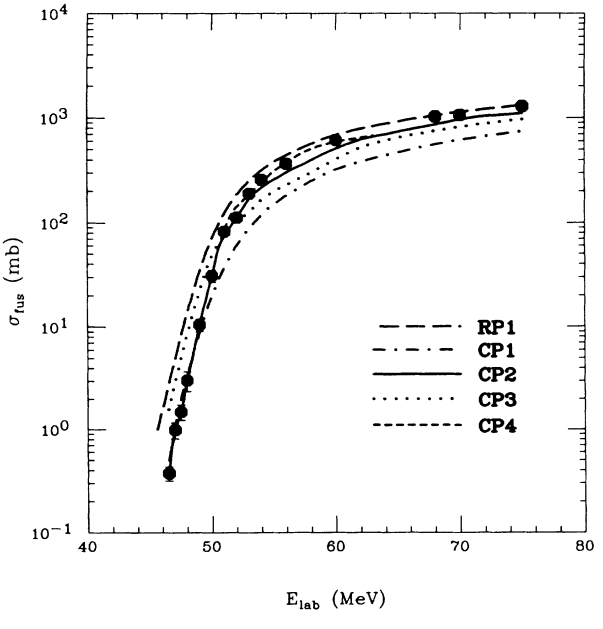

FIG. 4. Measured fusion cross sections as a function of bombarding energy for $^{12}C+^{144}Sm$. The different curves correspond to different optical-model potentials as described in the text.

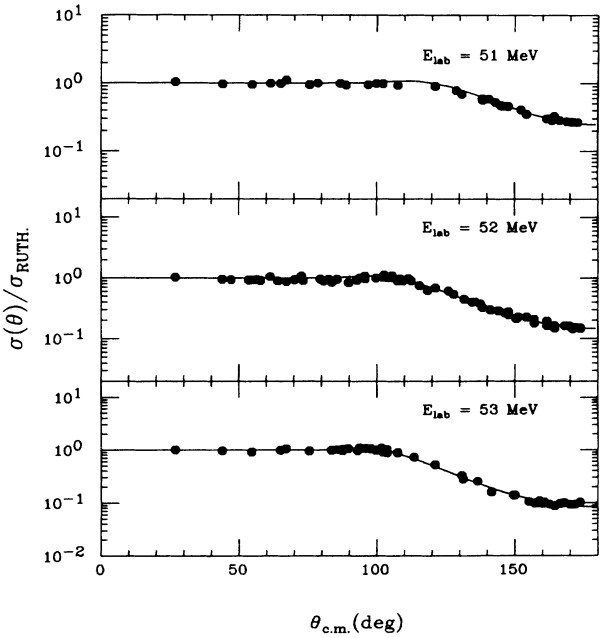

FIG. 6. Angular distributions for the elastic scattering of $^{12}C+^{144}Sm$ at $E_{lab}=51$, 52, and 53 MeV. The solid line is the optical-model fit (CP2).

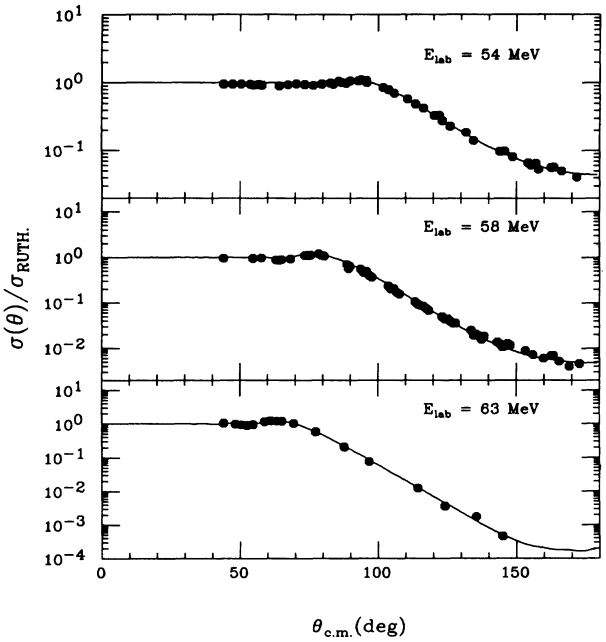

FIG. 7. Angular distributions for the elastic scattering of $^{12}C+^{144}Sm$ at $E_{lab}=54$, 58, and 63 MeV. The solid line is the optical-model fit (CP2).

III. OPTICAL MODEL

In the framework of the optical model, a potential that could describe simultaneously the elastic scattering and the fusion data was searched for. The potential had three terms, one real and two imaginary:

$$U(r)=VF(r,r_0,a)+iWF^2(r,ri_0,ai)+i4WSasi\frac{dF}{dr}(r,rsi_0,asi)\ , \tag{3}$$

where

$$F(x,x_0,\alpha)=\frac{1}{1+\exp[(x-X_0)/\alpha]}\ , \tag{4}$$

being $X_0=x_0(A_p^{1/3}+A_t^{1/3})$ and A_p and A_t the projectile and target mass numbers, respectively. The imaginary part that is proportional to the square of a Woods-Saxon potential [second term in expression (3)] simulates the incoming wave boundary condition and accounts for fusion. The other imaginary component is proportional to the derivative of a Woods-Saxon potential [last term in (3)] and takes into account peripheral (transfer and inelastic) reactions.

As in Ref. [1], the prescription of Rhoades-Brown *et al.* [9] was used for the volume part of the imaginary potential: $W=10$ MeV, $ri_0=1$ fm, and $ai=0.4$ fm. In what follows, the results of various fits to the data, obtained by varying the parameters V, r_0, a, WS, rsi_0, and asi using the code PTOLEMY [10], will be described. Fusion and peripheral reactions were evaluated using the method of Ref. [11]. Using a potential without an imaginary surface component ($WS=0$), the best fit of the elastic scattering data at $E_{lab}=51$, 52, 53, 54, 58, and 63 MeV yields the potential parameters: $V=106$ MeV, $r_0=1.29$ fm, $a=0.378$ fm with an average χ^2/ point of 1.22 (potential RP1). However, with these parameters the fusion cross sections are overestimated as shown in Fig. 4. Introducing an energy-independent imaginary surface potential different from zero, the potential parameters $V=228$ MeV, $r_0=1.18$ fm, $a=0.393$ fm, $WS=1.59$ MeV, $rsi_0=1.39$ fm, $asi=0.393$ fm (potential CP1) were obtained from fits to the elastic scattering date, with χ^2/point$=0.976$. Nevertheless, this potential underestimates the fusion cross sections (Fig. 4). If the restriction of using energy-independent potentials is removed, a potential (CP2) that describes simultaneously the fusion and the elastic scattering data is obtained. To evaluate the fusion cross sections at the highest energies ($E_{lab}=68$, 70, and 75 MeV) where no elastic data were available, it was assumed that the potential was the same as at $E_{lab}=63$ MeV. At lower energies ($E_{lab}=46.5$, 47, 47.5, 48, 49, and 50 MeV), it was assumed that $WS=0$ and V was varied in order to take into account fusion. The parameters of CP2 as a function of energy are presented in Table I. The comparison of the potentials at different energies is not simple since the potential shape changes. Hence, it is useful to observe the behavior of the potentials evaluated at the sensitivity radius R_s, i.e., the radial point where the elastic scattering is most sensitive. The sensitivity radius was evaluated at each energy (where angular distributions were available) as follows. The optimal potential was slightly modified changing the value of the diffusivity a. Then this parameter was fixed and the others were varied in order to fit the scattering data. This procedure was performed twice with values of a slightly smaller and larger than the optimum value. The radius at which the real parts of these potentials intercept one another is the sensitivity radius. It was observed that for all energies the potentials intercept each other in the region $11.1\ \text{fm}\le r\le 11.8$ fm and there was no appreciable variation of R_s with energy. Thus a value of $R_s=11.4$ fm was taken.

The real and imaginary parts of CP2 evaluated at R_s, V_{R_S}, and W_{R_S}, respectively, are displayed in Fig. 8. The variations in W_{R_S} are expected because inelastic and transfer channels are essentially closed for energies below the Coulomb barrier. In turn, the real part of the potential changes as a function of the energy through its correlation with the imaginary part given by the dispersion relation. The value of W_{R_S} was assumed to depend on the energy as follows:

$$W_{R_S}(E)=\begin{cases}0 \text{ for } E\le E_a\ ,\\ W_0(E-E_a)/(E_b-E_a) \text{ for } E_a<E<E_b\ ,\\ W_0 \text{ for } E\ge E_b\ ,\end{cases} \tag{5}$$

where the parameters E_a, E_b, and W_0 are varied to adjust the real potential $V_{R_S}(E)$ using the dispersion relations given in Ref. [12]:

$$V_{R_S}(E)=V_0+\delta V(E)\ , \tag{6}$$

TABLE I. Parameters of CP2 potential. At each energy, fusion cross section (σ_{fus}) and peripheral processes cross section (σ_{per}), obtained from these parameters, are tabulated. The projectile energy as well as V and WS are in MeV, radii and diffusivities in fm, and the cross sections in mb.

E_{lab}	V	r_0	a	WS	rsi_0	asi	χ^2/point	σ_{fus}	σ_{per}
46.5	180.0	1.19	0.426	0.00	0.00	0.00		0.44	0.00
47.0	203.0	1.19	0.426	0.00	0.00	0.00		0.93	0.00
47.5	203.0	1.19	0.426	0.00	0.00	0.00		1.69	0.00
48.0	203.0	1.19	0.426	0.00	0.00	0.00		3.01	0.00
49.0	220.0	1.19	0.426	0.00	0.00	0.00		10.58	0.00
50.0	236.0	1.19	0.426	0.00	0.00	0.00		30.86	0.00
51.0	333.0	1.19	0.426	0.61	1.46	0.157	0.473	88.41	29.31
52.0	364.0	1.19	0.428	1.62	1.46	0.157	0.584	118.5	81.68
53.0	462.0	1.19	0.414	1.46	1.46	0.157	0.709	178.6	98.94
54.0	442.0	1.19	0.417	1.23	1.46	0.157	0.433	236.0	106.5
58.0	367.0	1.18	0.438	1.18	1.46	0.144	0.733	428.8	149.5
63.0	256.0	1.20	0.426	0.69	1.46	0.157	1.170	678.8	132.7

with

$$\delta V(E)=\frac{W_0}{\pi}[\epsilon_a \ln|\epsilon_a|-\epsilon_b \ln|\epsilon_b|] , \tag{7}$$

where

$$\epsilon_i=\frac{E-E_i}{E_b-E_a} . \tag{8}$$

The solid lines in Fig. 8 are the predictions of Eq. (7) with $E_a=51.5$ MeV, $E_b=55.0$ MeV, and $W_0=0.5$ MeV. From this figure we conclude that the changes in V_{R_S} and W_{R_S} are qualitatively described by the dispersion relations. Using a different energy dependence of W_{R_S}, there is a somewhat better agreement with the real part of the potential (see dashed lines of Fig. 8). In this case, however, W_{R_S} increases at high energies while the data points are decreasing.

In order to test whether a good description of the data could be obtained allowing only one part of the potential to change with energy, two new potentials were introduced (CP3 and CP4); the first one keeps the real part (equal to that obtained at 51 MeV) fixed, and the imaginary part is varied to fit the scattering data. The second one keeps the imaginary part (equal to that of 63 MeV) fixed and the real part is varied. In both cases, for $E_{lab} \leq 50$ MeV we took $WS=0$. The new values of V_{R_S} and W_{R_S} are shown in Fig. 9 and neither one of them is

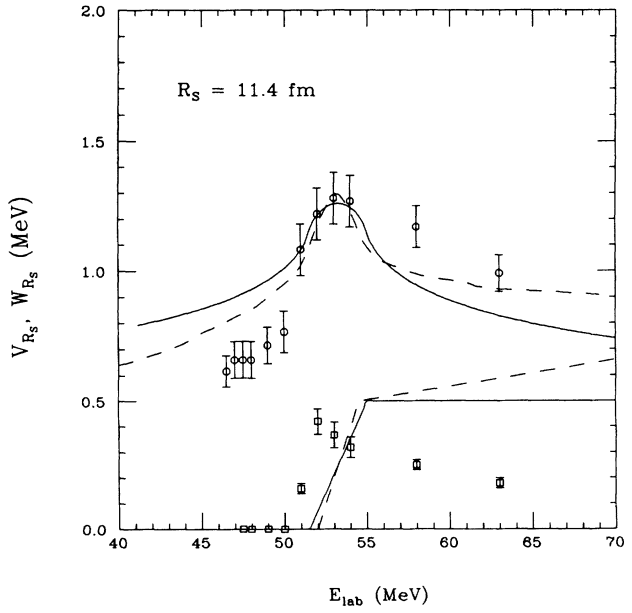

FIG. 8. Real (circles) and imaginary (squares) parts of the potential CP2, evaluated at the sensitive radius, as a function of the energy. The curves are the prediction of the dispersion relations.

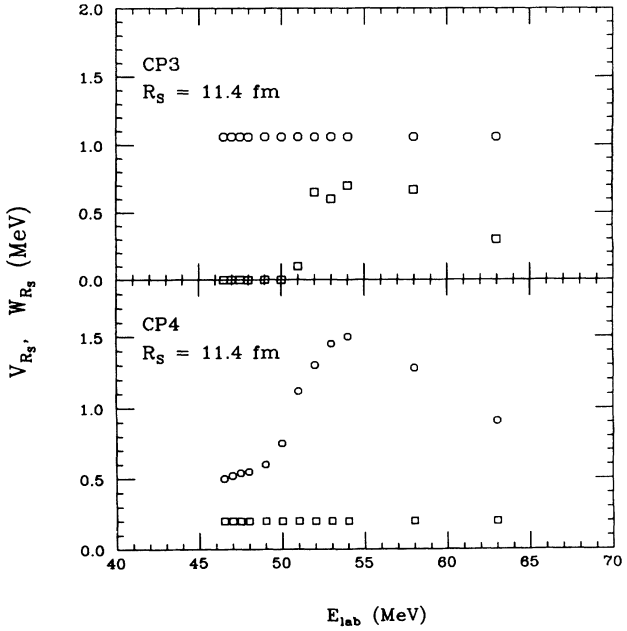

FIG. 9. Real (circles) and imaginary (squares) parts of the potentials CP3 and CP4, evaluated at the sensitive radius, as a function of the energy.

as good as CP2 in reproducing the fusion data (Fig. 4). However, the discrepancies are not so significative as those obtained with either RP1 or CP1. Thus it might be concluded that allowing an energy dependence of only one part of the potential the agreement with the fusion data is slightly worse. It is interesting to note that the part of the potential that was free to move behaves similarly to that obtained when both parts are varied. The main differences among those potentials (CP2, CP3, and CP4) are the predictions of peripheral reactions.

IV. SUMMARY AND CONCLUSIONS

Fusion and elastic scattering data for the $^{12}C+^{144}Sm$ system have been measured around the Coulomb barrier. These data were used to obtain the parameters of an energy-dependent optical-model potential. It was found that several potentials, with a wide variety of parameters, may describe the angular distributions, but only a few can reproduce the fusion cross section data. To describe at the same time the elastic scattering and the fusion data it was necessary that each part of the potential, real and imaginary, was variable with the energy and consistent with the dispersion relations. The agreement with the dispersion relations is only qualitative. Indeed, if the parametrizations of the imaginary part are forced to adjust the data points, then the calculated potential curve for the real part would be in worse correspondence with the data.

This result is similar to that obtained for the system $^{16}O+^{144}Sm$ in Ref. [1]. Moreover, the parameters of the dispersion relations that specify the changes in V_{R_S} are very similar in both systems.

With the potential obtained in the present analysis it is possible to predict the cross sections of inelastic and transfer reactions. The measurement of these channels, in progress in this laboratory, will determine the surface-imaginary potential more accurately and will be used as a test of the present description.

ACKNOWLEDGMENTS

We want to thank M. Elgue and F. Saporiti for their participation at the beginning of the experiments. We also want to thank R. Vandenbosch for reading the manuscript and making valuable comments. This work was supported in part by the Consejo Nacional de Investigaciones Científicas y Técnicas, CONICET, Argentina. A.A.S., A.E., M.C.E., J.O.F.N., A.J.P., and J.E.T. are members of the Consejo Nacional de Investigaciones Científicas y Técnicas, Argentina.

[1] D. Abriola, D. DiGregorio, J. E. Testoni, A. Etchegoyen, M. C. Etchegoyen, J. O. Fernández Niello, A. M. J. Ferrero, S. Gil, A. O. Macchiavelli, A. J. Pacheco, and J. Kittl, Phys. Rev. C **39**, 546 (1989).

[2] R. V. F. Janssens, R. Holzmann, W. Henning, T. L. Khoo, K. T. Lesko, G. S. F. Stephans, D. C. Raddord, and A. M. Van Den Berg, Phys. Let. B **181**, 16 (1986).

[3] D. DiGregorio, J. O. Fernández Niello, A. J. Pacheco, D. Abriola, S. Gil, A. O. Macchiavelli, J. E. Testoni, P. R. Pascholati, V. P. Vanin, R. Liguori Neto, N. Carlin Filho, M. M. Coimbra, P. R. S. Gomes, and R. G. Stokstad, Phys. Lett. B **176**, 322 (1986).

[4] D. DiGregorio, M. diTada, D. Abriola, M. Elgue, A. Etchegoyen, M. C. Etchegoyen, J. O. Fernández Niello, A. M. J. Ferrero, S. Gil, A. O. Macchiavelli, A. J. Pacheco, J. E. Testoni, P. R. Silveira Gomes, V. R. Vanin, R. Liguori Neto, E. Crema, and R. G. Stokstad, Phys. Rev. C **38**, 2124 (1988).

[5] F. Riess, private communication.

[6] C. M. Lederer and V. Shirley, *Table of Isotopes* (Wiley, New York, 1978).

[7] U. Reus and W. Westmeier, At. Data Nucl. Data Tables **29**, 194 (1983).

[8] A. J. Pacheco, D. E. DiGregorio, J. O. Fernández Niello, and M. Elgue, Comput. Phys. Commun. **52**, 93 (1988).

[9] M. J. Rhoades-Brown and P. Braun-Munzinger, Phys. Lett. **136B**, 19 (1984).

[10] M. J. Rhoades-Brown, M. H. MacFarlane, and S. C. Pieper, Phys. Rev. C **21**, 2417 (1980).

[11] J. A. Kittl, J. E. Testoni, A. O. Macchiavelli, A. J. Pacheco, D. Abriola, D. E. DiGregorio, A. Etchegoyen, M. C. Etchegoyen, J. O. Fernández Niello, A. M. J. Ferrero, and S. Gil, Nucl. Phys. **A471**, 587 (1987).

[12] C. Mahaux, N. Ngo, and G. R. Satchler, Nucl. Phys. **A449**, 354 (1986).